

Photocatalytic CO₂ reduction by Ni-substituted polyoxometalates: Structure-activity relationships and mechanistic insights



Khadija Talbi ^a, Francesc Penas-Hidalgo ^b, Amanda L. Robinson ^b, Philipp Gotico ^c, Winfried Leibl ^c, Pierre Mialane ^a, Maria Gomez-Mingot ^b, Marc Fontecave ^b, Albert Solé-Daura ^{d,*}, Caroline Mellot-Draznieks ^{b,*}, Anne Dolbecq ^{a,*}

^a Université Paris-Saclay, UVSQ, CNRS UMR 8180, Institut Lavoisier de Versailles, 78000 Versailles, France

^b Laboratoire de Chimie des Processus Biologiques, CNRS UMR 8229, Collège de France, Sorbonne Université, PSL Research University, 11 Place Marcelin Berthelot, 75231 Paris Cedex 05, France

^c Université Paris-Saclay, CEA, CNRS, Institute for Integrative Biology of the Cell (I2BC), 91198 Gif-sur-Yvette, France

^d Departament de Química Física i Inorgànica, Universitat Rovira i Virgili, Marcel·lí Domingo 1, 43007 Tarragona, Spain

ARTICLE INFO

Keywords:

Polyoxometalates
Ni substitution
Homogeneous photocatalysis
CO₂ reduction
DFT calculations

ABSTRACT

The photocatalytic activity for CO₂ reduction of a series of Ni-substituted polyoxometalates (POMs) differing in nuclearity, shape and size, has been investigated under visible light irradiation, with [Ru(bpy)₃]²⁺ (bpy = 2,2'-bipyridine) as photosensitizer and triethanolamine as sacrificial donor. The tetrabutylammonium salt of the Ni₄ tetrานuclear species was found to exhibit the highest CO production and its stability under photocatalytic conditions was demonstrated. The catalytic performance was significantly lower for the alkaline salt due to the separation of the POM from its counter-ions occurring only for the tetrabutylammonium salt. Photophysical experiments evidenced a bimolecular electron transfer from the reduced photosensitizer [Ru(bpy)₃]⁺ to the Ni₄ POM, the former arising from the reductive quenching of the [Ru(bpy)₃]²⁺ excited state by triethanolamine. This was further supported by DFT calculations, which also showed that the Ni₄ POM accumulates at least two electrons and four protons to carry out the CO₂ reduction catalytic process.

1. Introduction

Polyoxometalates (POMs) are described as molecular oxides based on high-valent metal (M) centers (W^{VI}, Mo^{VI}, V^{IV,V}...) that form MO_x (x = 5,6) polyhedral building units. They can incorporate heteroelements (P^V, Si^{IV}, Ge^{IV}, etc.) and transition metal centers (Fe, Co, Ni, Cu, Zn, etc.) in their structure and they can be further functionalized by organic ligands [1–5]. Besides their high tunability, they exhibit high thermal stability and have the ability to carry out multiple electron and proton transfers, which make them particularly attractive in the field of multi-electron-proton catalysis [6]. Furthermore, these molecular objects may be easily immobilized in various matrices such as metal-organic frameworks [7–9], leading to efficient heterogeneous catalysts.

In the field of solar energy conversion, POMs have been widely studied for photocatalytic proton reduction and water oxidation [10–14], while there are notably fewer reports on their use for CO₂ photoreduction [15,

16] and electroreduction [17–19]. Focusing on CO₂ to CO photoconversion, we can observe a few striking examples. In 2010, Neumann and coworkers showed for the first time that a POM substituted by a Ru^{III} center can catalyze CO₂ reduction with tertiary amines as sacrificial reducing agents [20]. In 2016, hybrid compounds with Re^I complexes associated to the Keggin-type PW₁₂ polyoxotungstate were prepared and a reaction pathway involving the reduced and protonated POM was proposed for the photoreduction of CO₂ [21]. Two years later, a high-nuclear mixed vanadium and cobalt oxo cluster-containing POM showed photocatalytic activity for CO₂ conversion [22]. This study involved for the first time a noble-metal-free POM and was followed by three studies dedicated to the use of homometallic nickel POMs as catalytic species. In 2021, Li, Zheng, Yang and coworkers described the photocatalytic activity of nickel cluster substituted silicotungstates [23]. One year later, Weinstock and coworkers showed that a large molecular assembly of ten hexaniobate POMs encapsulating a {Ni₃₀} cluster can act as an efficient photocatalyst for the reduction of CO₂, with water serving

* Corresponding authors.

E-mail addresses: albert.sol@urv.cat (A. Solé-Daura), caroline.mellot-draznieks@college-de-france.fr (C. Mellot-Draznieks), anne.dolbecq@uvsq.fr (A. Dolbecq).

as electron donor [24]. Finally, Fang and coworkers reported the same year the photocatalytic reduction of CO₂ with catalytic units consisting of self-assembled molecular cages built from {SiW₉Ni₄} units connected by rigid dicarboxylate linkers using [Ru(bpy)₃]²⁺ (bpy = 2,2'-bipyridine) complexes as photosensitizers [25]. In addition to these investigations of the catalytic activity of molecular POMs under homogeneous conditions, a few POM-based nanostructures have been studied for heterogeneous photocatalytic CO₂ reduction [26], often based on reduced polyoxomolybdate (i.e., containing Mo^V ions) structures [27–30]. Composites with Keggin type POMs encapsulated in Cd-based MOFs have also been reported as high-efficient CO₂ reduction catalysts [31]. However, there is still no clear evidence of the structural and compositional parameters that are important for the CO₂ to CO conversion catalytic activity of POMs.

As Ni-substituted compounds are among the most efficient POMs for photocatalytic proton reduction [32–38], and considering the recent reports of their activity for CO₂ reduction [23–25], we decided to investigate the catalytic properties of a series of Ni-based POMs with vacant {SiW₉} or {PW₉} units connected to Ni clusters (Fig. 1). The [(SiW₉O₃₄)Ni₄(CH₃COO)₃(OH)₃]⁸⁻ (**Ni₄Ac**) [39], [Ni₄(H₂O)₂(PW₉O₃₄)₂]¹⁰⁻ (**Ni₄**) [32], [{(PW₉O₃₄)Ni₃(OH)(H₂O)₂O₃PC(O)(C₃H₆NH₃)PO₃}₂Ni]¹⁴⁻ (**Ni₇**) [40], [(SiW₉O₃₄)Ni₁₄H₅(O₃PC(O)(C₃H₆NH₃)PO₃)₇(H₂O)₁₁(OH)₇]¹²⁻ (**Ni₁₄**) [36] and Ni[{(SiW₉O₃₄)Ni₄(OH)₃}₄(OOC(C₄H₂O)COO)₆]³⁰⁻ (**Ni₁₇**) [25] POMs were selected for this study. These POMs exhibit various Ni contents, sizes, charges and shapes and possess P or Si as heteroelement. These five POMs crystallize with ammonium and/or alkaline counter-ions (see experimental section). In order to study the influence of the nature of the counter-ions, the tetrabutylammonium (TBA) salt of Ni₄((TBA)Ni₄) [32] was also studied as well as the bis(triphenylphosphoranylidene)ammonium (P₂N) salt of Ni₁₄((P₂N)Ni₁₄) [36]. The photocatalytic proton reduction properties have been previously reported for both ((TBA)Ni₄) [32] and (P₂N)Ni₁₄) [36] and, as mentioned above, Ni₁₇ has been proven to be a good catalyst for the photocatalytic reduction of CO₂ [25]. Here, it serves as a reference compound. After optimization of the photocatalytic conditions (solvent, nature and concentration of the photosensitizer and the sacrificial donor), the catalytic activities of the seven aforementioned POM salts were investigated. Finally, photophysical measurements and DFT calculations were conducted on the Ni₄ catalyst, which exhibits the highest catalytic activity amongst the tested POMs in order to gain insights into the mechanism that governs the catalytic reaction.

2. Experimental section

2.1. Materials and instrumentation

All reagents were purchased from commercial sources and used as received. Infrared (IR) spectra were recorded on a Nicolet 30 ATR 6700 FT spectrometer. Thermogravimetry analyses (TGA) were performed on a Mettler Toledo TGA/DSC 1, STARe System apparatus under oxygen flow (50 mL min⁻¹) at a heating rate of 5 °C min⁻¹ up to 700 °C. EDX experiments were performed with a Jeol JSM-5800LV Scanning Microscope. Dynamic Light Scattering (DLS) experiments were performed on a Malvern Zetasizer Nano ZS. Electrospray ionization (ESI) mass spectra were recorded on a Xevo QT of WATERS (quadrupole-time-of-flight) instrument. The temperature of the source block was set to 120 °C, and the desolvation temperature was set to 200 °C. A capillary voltage of 1 kV was used in the negative scan mode, and the cone voltage was set to 10 V to control the extent of fragmentation of the identified species. Mass calibration was performed using a solution of sodium formate in water/acetonitrile (2:8) from *m/z* = 50 to 3000. Sample solutions were injected via a syringe pump directly connected to the ESI source at a flow rate of 20 μL/min.

2.2. Synthesis of POMs

The Ni-substituted polyoxotungstates Na₁₅[Na{(SiW₉O₃₄)Ni₄(CH₃COO)₃(OH)₃}₂]·4NaCl·36H₂O (**Ni₄Ac**) [39], Na₂K₈[Ni₄(H₂O)₂(PW₉O₃₄)₂]·28H₂O (**Ni₄**) [32], (TBA)₇H₃[Ni₄(H₂O)₂(PW₉O₃₄)₂]·4H₂O ((TBA)Ni₄) [32], Na₇K₇[{(PW₉O₃₄)Ni₃(OH)(H₂O)₂O₃PC(O)(C₃H₆NH₃)PO₃}₂Ni]₃·34H₂O (**Ni₇**) [40], Na₁₂[(SiW₉O₃₄)Ni₁₄H₅(O₃PC(O)(C₃H₆NH₃)PO₃)₇(H₂O)₁₁(OH)₇]·7H₂O (**Ni₁₄**) [36], (P₂N)₃₆H₃₀₈Na₄[(-SiW₉O₃₄)Ni₁₄(AleOH)₅(AleO)₂(H₂O)₁₁(OH)₇]·60H₂O ((P₂N)Ni₁₄) [36] and (NH₄)₂₂Na₈Ni[{(SiW₉O₃₄)Ni₄(OH)₃}₄(OOC(C₄H₂O)COO)₆]₁₅H₂O (**Ni₁₇**) [25] were synthesized according to reported procedures. These POMs were characterized in the solid state by IR spectroscopy and EDX measurements and the number of crystallization water molecules was confirmed by TGA measurements (Fig. S1).

2.3. Photocatalytic experiments

All photocatalytic experiments, except the kinetic and labelling experiments on (TBA)Ni₄ (vide infra), were run in a CH₃CN:H₂O:TEOA

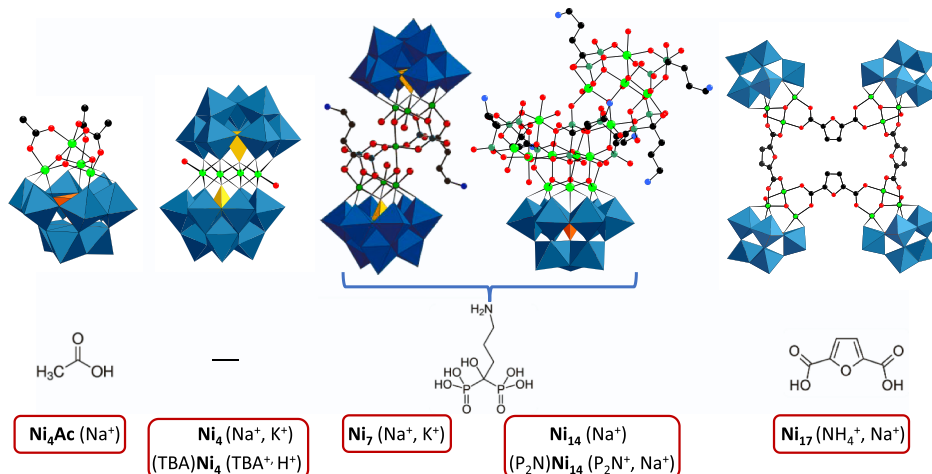


Fig. 1. Mixed polyhedral and ball-and-stick representation of the Ni-substituted POMs whose photocatalytic activities have been investigated in this study, with the formula of the organic ligand for the hybrid compounds, the abbreviation of the POM salts and the nature of the counter-ions in parentheses. Blue octahedra: WO₆, orange tetrahedra: SiO₄, yellow tetrahedra: PO₄, green spheres: Ni, red spheres: O, black spheres: C, blue spheres: N. Hydrogen atoms have been omitted for clarity.

(1.5 mL:0.33 mL:0.17 mL; TEOA = triethanolamine) solution with 0.06 μmol of POM and 3.9 μmol of $[\text{Ru}(\text{bpy})_3]\text{Cl}_2$, corresponding to the following concentrations: 30 μM of POM, 0.64 M of TEOA, 1.95 mM of $[\text{Ru}(\text{bpy})_3]\text{Cl}_2$. Photochemical reactions were performed using a 280 W, high-pressure Xe arc lamp (Newport Instruments). The beam was passed through a water infrared filter, a collimating lens, and a filter holder equipped with a 415 nm band-pass filter (Asahi Spectra). Samples were saturated with CO_2 via directly bubbling CO_2 through the solution mixture for 30 min. During irradiation, the samples were vigorously stirred at a controlled temperature (20 °C) and aliquots of the headspace were analyzed in two gas chromatographs (GCs). H_2 measurements (aliquots of 50 μL of the headspace) were performed by gas chromatography on a Shimadzu GC-2014 equipped with a Quadrex column and a Thermal Conductivity Detector and using N_2 as a carrier gas. CO was measured using a Shimadzu GC-2010 Plus carried by helium and with a S9 Restek ShinCarbon column and a flame ionization (FID) detector with a methanizer. Aliquots of gas were removed with a gas-tight syringe. Formate in the liquid phase was also analyzed using a Metrohm 883 Basic IC plus ionic exchange chromatography instrument, using a Metrosep A Supp 5 column and a conductivity detector. The sample was 100-fold diluted in deionized 18 MΩ water and 20 μL were injected into the IC chromatograph. No significant formate production was detected in all experiments. Calibration curves for H_2 and CO in a CO_2 matrix (0–70000 ppm) and for HCOOH in water (0–30 μM) were performed before analysis.

Kinetic measurements during photocatalysis were performed with blue LED irradiation (SugarCube LED lamp, emission at 463 nm with FWHM of 50 nm, 100 W m⁻² irradiation). Gaseous products were detected by automatic injection into a Micro GC Fusion Gas Analyzer, equipped with PLOT molecular sieve column, Ar carrier gas, and TCD detector. Mass spectrometry coupled to GC (Trace GC Ultra/ISQ, Thermo Scientific) was used for labelling experiments with ¹³ CO_2 .

2.4. Photophysical experiments

Transient absorption and emission experiments were performed on an Edinburgh Instruments LP920 Laser Flash Photolysis Spectrometer. The system incorporated a Continuum Q-switched Nd:YAG laser operating at 355 nm and a Continuum Surelite OPO for sample excitation at 460 nm (5 ns pulse duration, typical energy 7–10 mJ). The LP920 system is equipped with a 450 W Xenon lamp as the probe for the transient absorption measurements. Detection in the LP920 system is performed either via a Czerny-Turner blazed 500 nm monochromator (bandwidth: 1–5 nm) coupled with a Hamamatsu R928 photomultiplier tube (kinetics mode), or via a 500 nm blazed spectrograph (bandwidth: 5 nm) coupled with a water-cooled ICCD camera (Andor DH720; spectral mode). Samples, having absorbances of 0.6 at the excitation wavelength, were purged with argon prior to each experiment. The turnover number (TON) is defined as:

TON = Total mole number of product / Total mole number of catalyst.

2.5. Computational details

DFT calculations were carried out at the ω B97X-D level using Gaussian16 (rev C.02) quantum chemistry package [41]. The LANL2DZ basis set and associated pseudopotentials [42] were used to describe Ni and W atoms. These were supplemented by a Frenking's f-type polarization function [43]. The remaining atoms were described with the all-electron 6–31 g(d,p) basis set [44–46]. As the POM catalyst was experimentally found to remain in the aqueous phase during photocatalytic experiments (vide infra), solvent effects of water were included by means of the IEF-PCM implicit solvent model [47] as implemented in Gaussian16. Geometry optimizations were carried out without any symmetry restriction. The nature of all stationary points on the potential energy surface was confirmed by frequency calculations. The

standard-state correction of + 1.9 kcal mol⁻¹ (from the 1 atm reference state assumed in Gaussian calculations to the standard state of 1 mol L⁻¹ in solution at 25 °C) was applied to the free energy of all the species with the exception of water molecules. For the latter, which are part of the solvent, the standard-state correction accounts for + 4.3 kcal mol⁻¹ according to their concentration of 55.3 mol L⁻¹. A data set collection of the optimized structures for the most relevant species is available in the ioChem-BD repository [48] and can be accessed via 10.19061/iochem-bd-6–293.

3. Results and discussion

3.1. Photocatalytic reduction of CO_2

Photocatalytic experiments were performed in $\text{CH}_3\text{CN}:\text{H}_2\text{O}:\text{TEOA}$ solutions, with TEOA as sacrificial electron donor (SED), H_2O as proton source and $[\text{Ru}(\text{bpy})_3]^{2+}$ as photosensitizer (PS). The solutions were saturated with CO_2 and irradiated with a 280 W Xe lamp ($\lambda > 415$ nm) and both gas and liquid phases were analyzed after 2 h. For all the POMs, only negligible amount of formate was detected in the liquid phase, while CO and H_2 were present and quantified in the gas phase. The experimental conditions were optimized on (TBA) Ni_4 that proved to be the most efficient catalyst (see below). We considered first the solvent composition ratios. There was an optimum CO production (2.89 μmol , Table S1, entry 2) for a $\text{CH}_3\text{CN}:\text{H}_2\text{O}:\text{TEOA}$ ratio equal to 8.8:2:1 which corresponds to a mixture of 1.5 mL of CH_3CN , 0.33 mL of H_2O and 0.17 mL of TEOA. When lower or higher TEOA volumes were added, the CO production decreased (Table S1, entries 1 and 3). The presence of water was found to be beneficial for the production of CO, with a significant decrease from 2.89 to 0.74 μmol in absence of water (Table S1, entry 4). We then studied the influence of the nature and concentration of the photosensitizer. With 1.95 mM PS concentration, the CO production was higher with $[\text{Ru}(\text{bpy})_3]^{2+}$ (2.89 μmol) when compared to $[\text{Ru}(\text{phen})_3]^{2+}$ (1.61 μmol) while only traces were detected with $[\text{Ir}(\text{dtbbpy})(\text{ppy})_2]^+$ (Table S2, entries 1–3). Furthermore, an optimum condition was found with $[\text{Ru}(\text{bpy})_2]^{2+}$ concentration of 1.95 mM, with lower CO productions observed when higher or lower concentrations were used (Table S2, entries 1, 4–6). Control experiments indicated that (TBA) Ni_4 was inactive with negligible CO production in the absence of CO_2 , light, PS, sacrificial electron donor, or catalyst (Table S3, entries 1–6).

The production of CO and H_2 was measured for the seven salts of Ni-substituted POMs using the optimized conditions (Fig. 2a, Table S4). As shown in Fig. 2a, the lowest CO production was observed for Ni_7 (0.65 μmol) and Ni_4Ac (1.08 μmol) while (TBA) Ni_4 exhibited the highest CO production (2.89 μmol), showing a higher activity than Ni_{17} under similar conditions used in this study. However, the CO production of this Ni_4 POM was far lower (1.70 μmol , Fig. 2a, Table S4) when used as a mixed Na^+ and K^+ salt instead of a TBA salt. The same trend, although less pronounced, was observed for Ni_{14} , for which the CO production was equal to 1.63 μmol as a sodium salt and 1.94 μmol as an organic soluble salt (P₂N salt). For all the POMs, the CO selectivity lies between 73% (for Ni_4Ac) and 89% (for (P₂N) Ni_{14}) (Table S4). Furthermore, the production of CO and H_2 of the $\text{Na}_8\text{H}[\text{PW}_9\text{O}_{34}]$ precursor measured using the same conditions (Table S4) is very low, evidencing that the Ni ions play a crucial role in the catalytic process.

As (TBA) Ni_4 exhibits the best performance, all further studies were performed on it. The CO and H_2 productions were studied for catalyst's concentration ranging from 5 to 30 μM (Fig. 2b, Table S1, entries 7, 6 and 2). The CO production increases from 1.06 to 2.89 μmol with a selectivity equal to 93% for the lowest concentration. As usually observed, the CO turnover number (TON) is higher at lower catalyst concentrations (105 for 5 μM and 48 for 30 μM solutions). Finally, kinetic measurements were performed on (TBA) Ni_4 using an automatized set-up with blue LED irradiation (Fig. 2c, Table S5). The CO production increased linearly for the first 2 h but leveled off after 4 h. This plateau

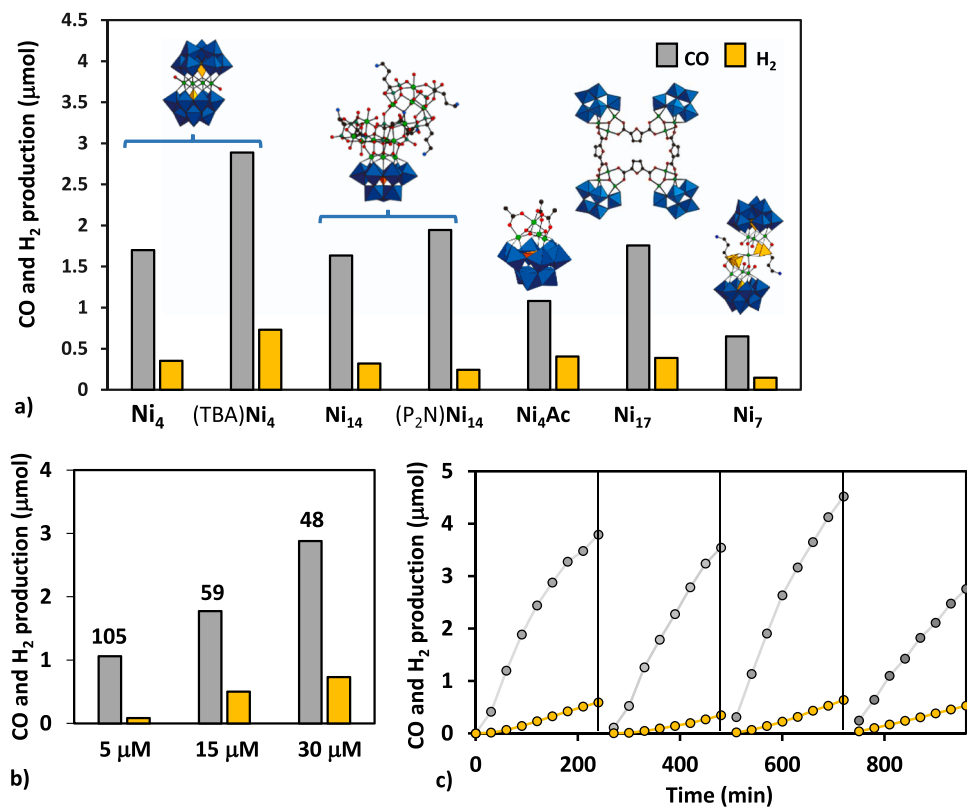


Fig. 2. CO (gray) and H₂ (yellow) production after 2 h for a CO₂-saturated solution of CH₃CN:H₂O:TEOA (1.5 mL:0.33 mL:0.17 mL) in the presence of 1.95 mM [Ru(bpy)₃]Cl₂ under visible light irradiation (280 W Xe lamp, $\lambda > 415$ nm) with (a) the various salts of Ni-substituted POMs (30 μ M) and (b) with various concentrations of the (TBA)Ni₄ POM (number labels indicate TONS); (c) time evolution of CO (gray line) and H₂ (orange line) production of (TBA)Ni₄ (30 μ M) under blue LED (463 nm) irradiation; additional 8.1 mg (10.8 μ mol) of [Ru(bpy)₃]₂Cl₂ were added after 240, 480 and 720 min showing the recovery of activity.

was attributed to the deactivation of the [Ru(bpy)₃]²⁺ photosensitizer, following the loss of a bipyridine linker [49–51]. The production restarted after addition of 8.1 mg (10.8 μ mol) of [Ru(bpy)₃]Cl₂. Four consecutive cycles have been done confirming that the plateau is not due to the degradation of the catalyst but to that of the photosensitizer. The CO production amounts to 14.6 μ mol after 16 h. In addition, an isotope tracer experiment was performed to determine the origin of CO. The peak at $m/z = 29$ observed in the mass spectrum (GC-MS) analysis of the gas generated from the photocatalytic reduction of ¹³CO₂ was assigned to ¹³CO, providing experimental proof that CO originates from CO₂ reduction (Fig. S2).

Strikingly, for all these photocatalytic experiments, a phase separation was observed (Fig. 3a), with a denser orange-colored phase (S2 solution) and a lighter colored phase at the top (S1 solution). This phase separation appears only after CO₂ bubbling. Salt-induced liquid-liquid phase separation in water-acetonitrile mixtures is a phenomenon commonly observed [52]. In the photocatalytic medium, ionic species are formed by CO₂ bubbling, such as zwitterionic TEOA-CO₂ adducts [53], carbamate, HTEOA⁺ and HCO₃⁻ species [44]. The presence of these ions alters the hydrogen-bond interactions between water and acetonitrile molecules, which contribute to the miscibility of these two solvents. Indeed, water molecules surround the ions, becoming unavailable for the organic solvent that becomes “salted out” from the aqueous phase [54]. The orange color of the S1 and S2 solutions indicates the presence of [Ru(bpy)₃]²⁺ in both phases. Furthermore, after separation of S1 and S2, addition of a large excess of [Ru(bpy)₃]Cl₂ in S2 leads to the formation of a precipitate for which the vibrational bands of the POM can clearly be identified (Fig. S3). On the contrary, no precipitate was observed after addition of [Ru(bpy)₃]Cl₂ in S1. It can be deduced that the POM is mainly present in the S2 phase.

Finally, ¹H NMR measurements performed on both phases of a

CD₃CN:D₂O:TEOA catalytic medium indicate that TEOA is present in both phases (two peaks at 3.40 and 2.69 ppm in S2 and 3.49 and 2.56 ppm in S1) and that the TBA cations are only present in the S1 phase (Fig. S4). We can further note that while the signals related to the TBA protons of the homogeneous catalytic solution obtained before bubbling CO₂ are broadened, indicating the presence of the paramagnetic POMs, they are well-defined in the ¹H NMR spectrum of S1, confirming that the POMs are only in the S2 phase. Moreover, we have noticed that the addition of a few drops of DMF to the biphasic mixture also restores a homogeneous phase which is maintained upon further CO₂ bubbling (S3 solution, Fig. 3b). It can be proposed that such addition of DMF regenerates the interactions between solvent molecules, preventing the liquid-liquid phase separation.

All these observations prompted us to further investigate the respective photocatalytic activity of each solution. The photocatalytic activity of 2 mL of the S(1+2) solution vigorously agitated (usual conditions) have been compared to that of 2 mL of S1 and 2 mL of S2 separately and of 2 mL of S3 (Fig. 3c). As expected, the activity of the S1 solution is far lower than that of S(1+2) because the POM is mainly in the S2 solution. Even if all the components of the catalytic reaction are present in the S2 and S3 solutions, the catalytic activity of these two solutions is also lower than that of the S(1+2) solution. This can be expected for S2, knowing that the solubility of CO₂ is lower in H₂O than in CH₃CN, but is more surprising for S3. We also carried out two complementary experiments, one with just water and TEOA as the catalytic medium and the other with two drops of DMF added to the CH₃CN:H₂O:TEOA mixture, that thus remains biphasic (Fig. S5). The CO production dramatically drops when the catalysis is performed in the H₂O/TEOA mixture (~71%) whereas it is maintained when only two drops of DMF are added, in the CH₃CN:H₂O:TEOA mixture, which is still biphasic. These experiments show that DMF does not inhibit the catalytic reaction

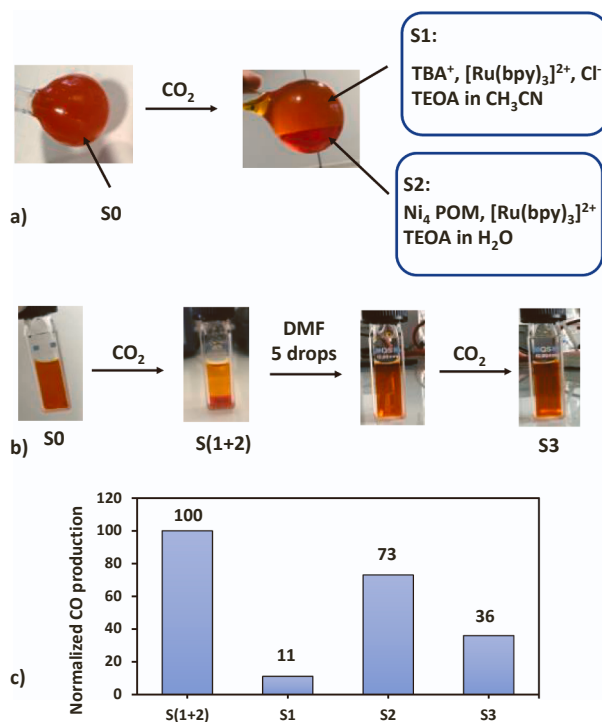


Fig. 3. Pictures of a) a 30 mL catalytic solution before and after bubbling CO₂; b) a 2 mL catalytic solution before and after bubbling CO₂ and after addition of DMF; c) normalized CO production of the various solutions. Catalytic conditions: 2 mL of CO₂-saturated solution irradiated during 2 h (280 W Xe lamp, $\lambda > 415$ nm).

and that the formation of a phase separation is essential. It can be proposed that the catalytic reaction takes place in the water phase at its interface with the CH₃CN phase and that the separation of the POM (in the S2 solution) from its TBA counter-ions (in the S1 solution) has a beneficial impact on the photocatalytic activity. This hypothesis is in line with the observation that the catalytic activity of the alkaline salt of Ni₄ is lower than that of (TBA)Ni₄ (Fig. 2a). Indeed, with the alkaline salt, the sodium and potassium counter-ions interact strongly with the Ni₄ POM and must remain close to it in the aqueous phase [55] and might hinder the catalytic process. The solutions after photocatalysis were analyzed by electrospray ionization mass spectrometry (ESI-MS). The peak attributed to the oxidized product of TEOA (aldehyde) was clearly visible on the mass spectrum of the aqueous phase S2 (Fig. S6), confirming the oxidation of TEOA during the catalytic process and its role as a sacrificial electron donor. We can note that such oxidation product of TEOA has been previously observed [56,57].

The stability of the catalyst is obviously an important parameter in photocatalytic CO₂ reduction. The IR spectrum of the precipitate obtained by addition of [Ru(bpy)₃]Cl₂ in S2 after photocatalysis is identical to that of the precipitate obtained before catalysis and also very similar to the IR spectrum of the pristine POM in the W-O, W=O and P-O vibrations regions (Fig. S3). EDX measurements performed on the precipitate obtained by addition of [Ru(bpy)₃]Cl₂ in S2 after photocatalysis have shown that the Ni/P and P/Ni ratio are the ones expected for a [Ni₄(H₂O)₂(PW₉O₃₄)₂]¹⁰⁻ POM (Ni/W ratio calc = 0.22, exp = 0.28; P/Ni ratio calc = 0.50, exp = 0.47). Furthermore, as mentioned above, the addition of [Ru(bpy)₃]Cl₂ allows to restore the CO production (Fig. 2c). Finally, dynamic light scattering (DLS) experiments indicate the absence of particles having a diameter higher than 1 nm, suggesting that no nickel oxide nanoparticle was formed during the catalytic event. All these observations support that (TBA)Ni₄ is stable under the described

catalytic conditions.

3.2. Mechanistic study of the (TBA)Ni₄ POM photocatalytic system

3.2.1. Photophysical studies

During photocatalysis, photon absorption creates the excited state of the photosensitizer that either interacts with the SED to form the long-lived reduced form [Ru(bpy)₃]⁺ (reductive quenching) which is then activating the catalyst, or reduces the catalyst (oxidative quenching) leading to formation of the strong oxidant [Ru(bpy)₃]³⁺ that is then reduced by the SED. To obtain more insight into the photocatalytic mechanism at work, we performed time-resolved photophysical studies. First, the interaction of the sacrificial electron donor TEOA with the [Ru(bpy)₃]²⁺ photosensitizer was studied. Addition of increasing amounts of TEOA up to 3 M hardly affects the kinetics of the [Ru(bpy)₃]²⁺ excited state (Fig. S7A) although the small bleaching of the MLCT absorption persisting after decay of the excited state indicated formation of the reduced form of the photosensitizer (Fig. S7B). This was confirmed by the observation of formation of a long-lived (\gg ms) species with absorption features characteristic of the reduced photosensitizer, [Ru(bpy)₃]⁺ (Fig. S8). Due to the low rate constant for quenching of the excited state by TEOA ($k_{\text{TEOA}} = 4 \cdot 10^4 \text{ M}^{-1}\text{s}^{-1}$) the quantum yield of formation of [Ru(bpy)₃]⁺ is low and amounts to around 3% for the concentrations of SED (0.64 M) typically used in the photocatalytic reactions (Fig. S9).

We then investigated the interaction between the excited state of the photosensitizer and the catalyst. When 10 μ M of (TBA)Ni₄ POM were added to a solution of 40 μ M [Ru(bpy)₃]²⁺, the emission of the latter was nearly completely quenched (Fig. S10). This is strong indication for formation of ion-pairing adducts between the highly negatively charged POM and the double positively charged photosensitizer. As the quenching of emission was much weaker in presence of only 3 μ M POM it can be concluded that one POM can fix around four photosensitizer complexes. This electrostatic interaction is also detectable as a redshift in the emission and absorption spectra of the photosensitizer (Fig. S11). The most likely pathway for deactivation of the excited state of the photosensitizer is via a fast and reversible electron transfer to the POM. However, this electron transfer does not lead to the formation of a charge-separated state sufficiently stable to be detectable on a nanoseconds time scale. The main reason could be that the [Ru(bpy)₃]³⁺ species formed after electron injection into the POM is even more strongly bound to the POM and unable to escape the association complex before charge recombination. This makes a photocatalytic reaction mechanism involving POM reduction from the photosensitizer excited state unlikely. However, it should be noted that with the large excess of photosensitizer over POM employed in the photocatalytic experiments (1.85 mM [Ru(bpy)₃]²⁺ for 10 μ M POM) only a negligible fraction of photosensitizer activity is lost due to scavenging by the POMs. The grand majority of PS molecules should show a long-lived excited state able to interact with the SED, forming the more reducing [Ru(bpy)₃]⁺ species with an efficiency as described above. This long-lived [Ru(bpy)₃]⁺ species is then the reductant for the catalyst.

Photophysical characterization was also performed on a three-component system comprising the photosensitizer, POM, and TEOA. It appears that the presence of TEOA at high concentration weakens the electrostatic interaction between the photosensitizer and the POM to some extent as in the presence of TEOA less static quenching of the photosensitizer excited state is observed (compare Fig. S12 and Fig. S10). Analysis of the amount of long-lived excited state as a function of concentration of POM (Figs. S12 and S13) allows to estimate that the POM can bind up to four equivalents of [Ru(bpy)₃]²⁺ complexes. Fig. 4 shows the kinetics of the reduced state of the (free) photosensitizer, recorded at 510 nm on a long-time scale, for different concentrations of POM. The traces show the fast formation of the [Ru(bpy)₃]⁺ state followed by its decay that is accelerated with increasing concentration of POM. This finding is a strong indication for the occurrence of

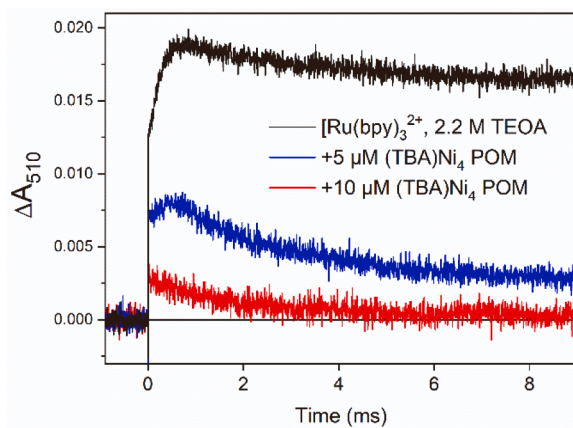


Fig. 4. Kinetics of transient absorption at 510 nm of $[\text{Ru}(\text{bpy})_3]^{2+}$ (40 μM) upon excitation with nanosecond laser flashes at 460 nm in Ar-saturated $\text{MeCN}/\text{H}_2\text{O}$ (9/1), 2.2 M TEOA solution containing increasing concentrations of (TBA) Ni_4 POM.

bimolecular electron transfer from the reduced photosensitizer to the POM, with a rate of about $6 \times 10^7 \text{ M}^{-1}\text{s}^{-1}$.

3.2.2. DFT calculations

To further investigate the interactions between the Ni_4 POM catalyst and the other components of the photocatalytic system under light irradiation, we next conducted theoretical DFT calculations. As the redox properties of POMs are strongly dependent on their protonation state [58], we firstly examined the ability of Ni_4 to associate protons under photocatalytic conditions. To this end, we considered the N-protonated form of TEOA (HTEOA^+) as the source of protons. With a pK_a of 7.8 [59], the latter is expected to exist in equilibrium with TEOA in the reaction mixture, but it is also generated through the spontaneous deprotonation of $\text{TEOA}^{\bullet+}$ radical cations that arise from the reductive quenching of the photoexcited $[\text{Ru}(\text{bpy})_3]^{2+}$, by a second TEOA molecule [57,60–62].

Under photocatalytic conditions, the Ni_4 catalyst was found to spontaneously abstract up to two protons from HTEOA^+ molecules, the reaction Gibbs free-energies for the first and the second proton transfer events being -6.8 and $-5.1 \text{ kcal mol}^{-1}$, respectively (Fig. S14). The protons in the doubly-protonated anion, labeled as H_2Ni_4 , are accommodated on two μ_2 -(Ni-O-W) bridging oxygen sites in an antisymmetric disposition, which grant the formation of stabilizing intramolecular hydrogen bonds with neighboring O sites of the POM framework, as shown in Fig. 5a. Further protonation of H_2Ni_4 by HTEOA^+ was

predicted to be thermodynamically unfavorable, by $4.2 \text{ kcal mol}^{-1}$ (Fig. S14). Thus, we next analyzed the feasibility of electron transfer events from the photosensitizer to H_2Ni_4 .

Fig. 5b compares the calculated Gibbs free energies associated to the reduction of the catalyst via single electron transfer (SET) following either oxidative quenching (red arrows) or reductive quenching (blue arrows) mechanisms. As anticipated above, the oxidative quenching pathway involves a SET from the triplet MLCT state of the photoexcited photosensitizer, (labeled as $[\text{Ru}(\text{bpy})_3]^{2+,*}$) to H_2Ni_4 , which was calculated to be endergonic by $15.3 \text{ kcal mol}^{-1}$. Even though this might be accessible at room temperature, the charge recombination between the reduced POM and the oxidized PS was found to be strongly favorable (by $64.5 \text{ kcal mol}^{-1}$), thus preventing the efficient formation of the reduced POM, as observed experimentally. Conversely, the one-electron reduced form of the photosensitizer, $[\text{Ru}(\text{bpy})_3]^+$, formed in the reaction mixture via reductive quenching of $[\text{Ru}(\text{bpy})_3]^{2+,*}$ by TEOA as evidenced experimentally (see above), can more efficiently reduce H_2Ni_4 through a SET process that was estimated to be ergoneutral. Therefore, these results strongly indicate that the $\text{Ni}_4/[\text{Ru}(\text{bpy})_3]^{2+}/\text{TEOA}$ photocatalytic system operates through a reductive quenching mechanism (Fig. 5b, blue arrows), further supporting the mechanistic picture inferred from photophysical studies. It is worth noting that protonation of the Ni_4 is essential to allow efficient charge accumulation in the catalyst. As a matter of fact, the SET from $[\text{Ru}(\text{bpy})_3]^+$ to the non-protonated Ni_4 , which bears an overall charge of -10 , is much less favorable compared to that to the doubly-protonated $[\text{H}_2\text{Ni}_4]^{8-}$ anion, with a reaction free-energy of $+16.9 \text{ kcal mol}^{-1}$ (vs. $0.0 \text{ kcal mol}^{-1}$). This can be ascribed to the polyanionic nature of the POM, as reducing its overall negative charge via protonation lowers the energy of its unoccupied Molecular Orbitals (MOs), favoring in turn reduction events [58]. It is also worth noting that possible ion-pairing effects involving the POM, which are not explicitly captured in our models, are expected to ease SET processes due to the same principle, although to a lesser extent than protonation [58]. Hence, it cannot be ruled out that the SET processes from the PS to the POM are actually somewhat more exergonic than what computed values suggest.

As shown in Fig. 5c, reduction of the catalyst by $[\text{Ru}(\text{bpy})]^+$ generates species $[\text{H}_2\text{Ni}_4(1e)]^{9-}$, in which the extra electron is accommodated in a d-type MO centered on a W atom of the polyoxotungstate framework, in line with previous studies on the redox properties of Ni(II)-substituted POMs [33]. Under photocatalytic conditions, $[\text{H}_2\text{Ni}_4(1e)]^{9-}$ can then accept a second electron from a $[\text{Ru}(\text{bpy})]^+$ molecule to yield $[\text{H}_2\text{Ni}_4(2e)]^{10-}$. Despite this process was computed to be slightly endergonic ($\Delta G_{\text{SET}} = +7.2 \text{ kcal mol}^{-1}$, Fig. S14), the subsequent, spontaneous association of two more protons to μ_2 -(Ni-O-W) sites (ΔG of -15.0 and $-7.9 \text{ kcal mol}^{-1}$ for the protonation of $[\text{H}_2\text{Ni}_4(2e)]^{10-}$

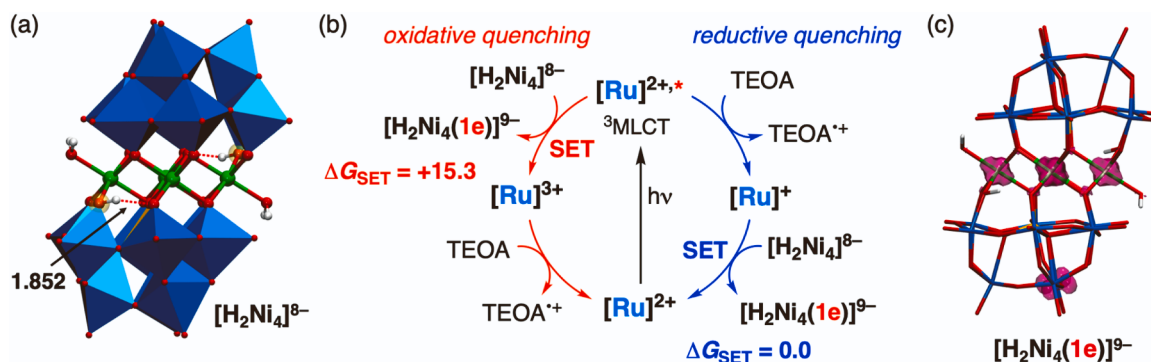


Fig. 5. (a) Combined polyhedral and balls-and-sticks representation of the optimized structure of H_2Ni_4 . Protonated μ_2 -(Ni-O-W) bridging oxygens are highlighted with semi-transparent yellow spheres. Red-dashed lines highlight intramolecular hydrogen bonds, for which a selected distance is given in \AA . (b) Comparison of the reaction free-energies (kcal mol^{-1}) for the single electron transfer (SET) processes governing the reduction of the catalyst via oxidative quenching (left, red arrows) and reductive quenching (right, blue arrows) mechanisms (see main text for details). (c) Spin density distribution represented on the optimized structure of $[\text{H}_2\text{Ni}_4(1e)]^{9-}$.

and $[\text{H}_3\text{Ni}_4(2e)]^{9-}$ by HTEOA⁺, respectively) provides the thermodynamic driving force for the second SET event and prevents undesired back electron transfer from the reduced POM to the PS. This sequence of reduction and protonation processes is highlighted with bold blue arrows in Fig. S14 and leads to species $[\text{H}_4\text{Ni}_4(2e)]^{8-}$, for which the optimized structure and spin density distribution are represented in Fig. S15. Overall, our calculations indicate that the photoaccumulation in the Ni₄ catalyst of the two electrons required for subsequent CO₂ to CO reduction is feasible following a reductive quenching mechanism. Moreover, the fact that the reduction of the catalyst triggers its protonation suggests that the POM might not only play the role of an electron reservoir but also that of a proton reservoir, making protons readily available for the protonation of key reaction intermediates.

From a thermodynamic point of view, the reduction of CO₂ to CO promoted by $[\text{H}_4\text{Ni}_4(2e)]^{8-}$, giving a water molecule as a byproduct and regenerating the fully-oxidized $[\text{H}_2\text{Ni}_4]^{8-}$ anion was computed to be slightly endergonic by 4.5 kcal mol⁻¹, although still affordable, while the reduction and protonation of $[\text{H}_2\text{Ni}_4]^{8-}$ to $[\text{H}_4\text{Ni}_4(2e)]^{8-}$, which is strongly exergonic ($\Delta G = -27.6$ kcal mol⁻¹, Fig. S14), might be expected to provide the thermodynamic driving force for the overall process. However, additional DFT calculations showed that the reduction of $[\text{H}_4\text{Ni}_4(2e)]^{8-}$ by a third electron is still accessible ($\Delta G_{\text{SET}} = +3.5$ kcal mol⁻¹, Fig. S14), thus implying that the latter process may be faster than the formation of CO catalyzed by $[\text{H}_4\text{Ni}_4(2e)]^{8-}$. Therefore, it cannot be ruled out that higher reduction states of the POM are formed during the course of the reaction and that they may also act as active species of the catalyst. In this regard, further computational and experimental efforts would be required to more precisely identify and characterize the active species responsible for the CO₂RR activity of Ni-POMs which is, however, beyond the scope of the present study.

Still, with the gained knowledge about the Ni₄/[Ru(bpy)₃]²⁺/TEOA photocatalytic system and on the basis of previously reported reaction mechanisms for CO₂ reduction by transition-metal based compounds bearing redox-active ligands [63–71], we propose the following reaction mechanism illustrated in Fig. 6. Upon reduction and protonation of the catalyst by “n” electrons and “m” protons, respectively, the coordination of CO₂ through the C atom to a Ni(II) ion replacing an aqua ligand generates a Ni(II)-COO[•] species, in which one electron migrates from the POM to the CO₂ moiety. Up next, the protonation of a terminal O atom in the latter intermediate triggers the migration of a second electron from the POM to the reactive center leading to a Ni(II)-COOH species, which then evolves via concomitant C—O(H) bond cleavage and protonation of the leaving group to generate a water molecule. Finally, the replacement of the CO product by a water molecule, along with the reduction and protonation of the catalyst by [Ru(bpy)₃]⁺ and HTEOA⁺, respectively, which are generated through the light-induced reductive quenching of the PS by TEOA, as detailed in Fig. 5b (and simplified in Fig. 6 with a small blue cycle), regenerates the active species of the catalyst, closing the catalytic cycle.

4. Conclusions

In this work, the photocatalytic activities for visible-light driven CO₂ to CO conversion of seven POM salts with vacant {SiW₉} or {PW₉} units connected to Ni clusters have been investigated in CH₃CN:H₂O:TEOA solutions. This study confirms that Ni-based POMs are efficient catalysts and shows that the tetrabutylammonium salt of the POM containing four Ni(II) ions sandwiched between two {PW₉} units, TBA(Ni₄), was the most active, with a high selectivity and a good stability. While no clear trend was observed for the impact of the number of Ni ions or the nature and number of vacant POMs bound to these Ni ions, this study highlights the influence of the nature of the counter-ions on the catalytic activity of POMs, the TBA salt of Ni₄ being much more active than the alkaline salt. This observation was correlated with a phase separation that occurs after CO₂ bubbling into the catalytic medium. NMR and IR measurements indeed showed that the POM (in the aqueous phase) is separated

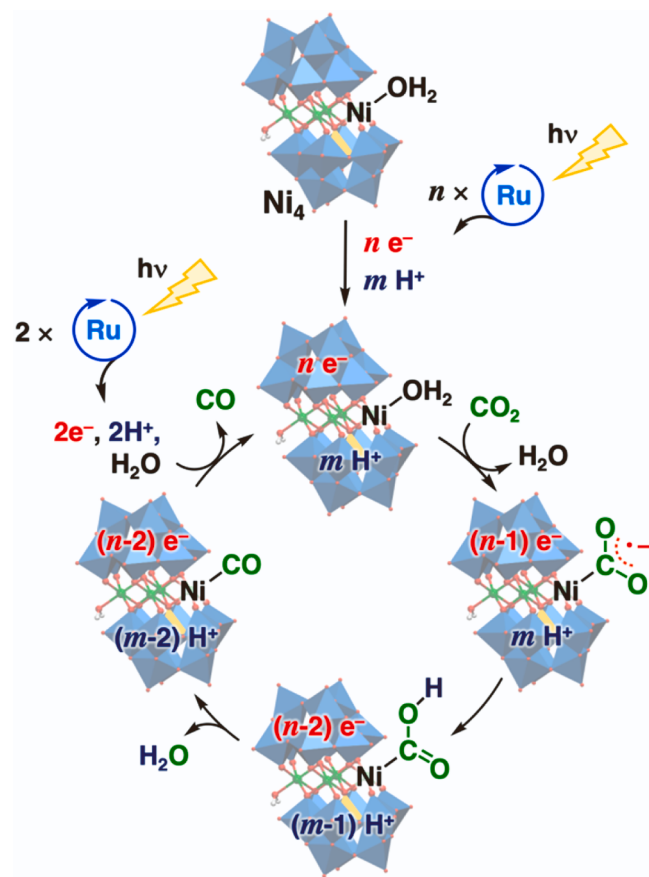


Fig. 6. Proposed reaction mechanism for the photocatalytic reduction of CO₂ into CO catalyzed by Ni₄ in the presence of [Ru(bpy)₃]²⁺ and TEOA acting as an external photosensitizer and sacrificial donor, respectively (see Fig. 5b for details).

from its TBA counter-ions (in the organic phase), which improves the catalytic activity. This opens perspectives for photocatalytic studies of POM compounds, as alkaline salts of POMs can often be easily converted to TBA ones. Focusing on the most active Ni₄ system, both transient absorption spectroscopy and DFT calculations support that the reduction of the catalyst by the [Ru(bpy)₃]²⁺/TEOA photochemical system proceeds via a reductive quenching pathway, whereby the excited triplet MLCT state of the PS is quenched by TEOA to generate the one-electron reduced [Ru(bpy)₃]⁺ species, which acts as the reducing agent of the Ni₄ catalyst. DFT calculations also indicate that the Ni₄ catalyst is spontaneously protonated by the HTEOA⁺ cations that are generated during the reductive quenching of the PS. Such protonation events are essential, enabling the reduction of the catalyst via electron transfer from [Ru(bpy)₃]⁺ by lowering the energy of the unoccupied molecular orbitals of the POM. Moreover, our calculations demonstrate that Ni₄ is capable of undergoing multiple redox processes under photocatalytic conditions, which lead to the accumulation of electrons in the POM for subsequent CO₂ reduction. These results allowed proposing a reaction mechanism in which the Ni(II) centers act as catalytically active sites and the polyoxotungstate framework acts as a reservoir of the electrons and protons needed for the reduction of CO₂ to CO.

CRediT authorship contribution statement

Mellot-Draznieks Caroline: Conceptualization, Funding acquisition, Methodology, Supervision, Writing – review & editing. **Dolbecq Anne:** Conceptualization, Funding acquisition, Project administration, Supervision, Writing – original draft, Writing – review & editing. **Talbi Khadija:** Data curation, Formal analysis, Investigation, Visualization.

Mialane Pierre: Conceptualization, Supervision, Writing – review & editing. **Gomez-Mingot Maria:** Validation, Writing – review & editing. **Fontecave Marc:** Resources, Validation, Writing – review & editing. **Solé-Daura Albert:** Conceptualization, Methodology, Supervision, Writing – original draft, Writing – review & editing. **Penas-Hidalgo Francesc:** Formal analysis, Investigation, Visualization. **Robinson Amanda Lyn:** Investigation, Validation, Writing – review & editing. **Gotico Philipp:** Data curation, Investigation, Writing – review & editing. **Leibl Winfried:** Data curation, Investigation, Writing – original draft.

Declaration of Competing Interest

The authors declare that they have no known competing financial interests or personal relationships that could have appeared to influence the work reported in this paper.

Data Availability

Data will be made available on request.

Acknowledgements

This work was supported by a grant of the Agence Nationale de la Recherche (ANR-21-CE50-0024). F. P.-H., A.S.-D. and C. M.-D. thank GENCI (CINES/TGCC) for HPC resources through the 2022–2023 grant A0130907343. CMD thanks ANR for funding ANR-21-CE07-0028. A.S.-D. also acknowledges the Spanish Ministry of Universities and the European Union - Next Generation EU for financial support through a Margarita Salas grant. A. D. thanks Julien Bonin for fruitful discussion. Aurélie Damond is gratefully acknowledged for mass spectrometry measurements.

Appendix A. Supporting information

Supplementary data associated with this article can be found in the online version at [doi:10.1016/j.apcatb.2023.123681](https://doi.org/10.1016/j.apcatb.2023.123681).

References

- [1] A. Dolbecq, E. Dumas, C.R. Mayer, P. Mialane, Hybrid organic–inorganic polyoxometalate compounds: from structural diversity to applications, *Chem. Rev.* 110 (2010) 6009–6048.
- [2] H. Zhang, W.-L. Zhao, H. Li, Q. Zhuang, Z. Sun, D. Cui, X. Chen, A. Guo, X. Ji, S. An, W. Chen, Y.-F. Song, Latest progress in covalently modified polyoxometalates-based molecular assemblies and advanced materials, *Polyoxometalates* 1 (2022) 9140011, <https://doi.org/10.26599/POM.2022.9140011>.
- [3] J.M. Cameron, G. Guillenot, T. Galambos, S.S. Amin, E. Hampson, K. Mall Haidaraly, G.N. Newton, G. Izzet, Supramolecular assemblies of organo-functionalised hybrid polyoxometalates: from functional building blocks to hierarchical nanomaterials, *Chem. Soc. Rev.* 51 (2022) 293–328, <https://doi.org/10.1039/D1CS00832C>.
- [4] P. Ma, F. Hu, J. Wang, J. Niu, Carboxylate covalently modified polyoxometalates: from synthesis, structural diversity to applications, *Coord. Chem. Rev.* 378 (2019) 281–309, <https://doi.org/10.1016/j.ccr.2018.02.010>.
- [5] A. Blazevic, A. Rompel, The Anderson–Evans polyoxometalate: from inorganic building blocks via hybrid organic–inorganic structures to tomorrow’s “Bio-POM”, *Coord. Chem. Rev.* 307 (2016) 42–64, <https://doi.org/10.1016/j.ccr.2015.07.001>.
- [6] S.-S. Wang, G.-Y. Yang, Recent advances in polyoxometalate-catalyzed reactions, *Chem. Rev.* 115 (2015) 4893–4962, <https://doi.org/10.1021/cr500390v>.
- [7] P. Mialane, C. Mellot-Draznieks, P. Gairola, M. Duguet, Y. Benseghir, O. Oms, A. Dolbecq, Heterogenisation of polyoxometalates and other metal-based complexes in metal–organic frameworks: from synthesis to characterisation and applications in catalysis, *Chem. Soc. Rev.* 50 (2021) 6152–6220, <https://doi.org/10.1039/D0CS00323A>.
- [8] M. Samaniyan, M. Mirzaei, R. Khajavian, H. Eshtiagh-Hosseini, C. Streb, Heterogeneous catalysis by polyoxometalates in metal–organic frameworks, *ACS Catal.* 9 (2019) 10174–10191, <https://doi.org/10.1021/acscatal.9b03439>.
- [9] C.T. Buru, O.K. Farha, Strategies for incorporating catalytically active polyoxometalates in metal–organic frameworks for organic transformations, *ACS Appl. Mater. Interfaces* 12 (2020) 5345–5360, <https://doi.org/10.1021/acsami.9b19785>.
- [10] J.-L. Chen, Z.-W. Wang, P.-Y. Zhang, H. Lv, G.-Y. Yang, 40Ni-added poly (polyoxometalate) assembled by $\{Ni_6GeW_9\}$ and $\{Ni_8(GeW_9)_2\}$ units: structure, magnetic, and heterogeneous catalysis properties, *Inorg. Chem.* 62 (2023) 10291–10297, <https://doi.org/10.1021/acs.inorgchem.3c01091>.
- [11] X.-B. Han, Z.-M. Zhang, T. Zhang, Y.-G. Li, W. Lin, W. You, Z.-M. Su, E.-B. Wang, Polyoxometalate-based cobalt–phosphate molecular catalysts for visible light-driven water oxidation, *J. Am. Chem. Soc.* 136 (2014) 5359–5366, <https://doi.org/10.1021/ja412886e>.
- [12] M.A. Fashapoyeh, M. Mirzaei, H. Eshtiagh-Hosseini, A. Rajagopal, M. Lechner, R. Liu, C. Streb, Photochemical and electrochemical hydrogen evolution reactivity of lanthanide-functionalized polyoxotungstates, *Chem. Commun.* 54 (2018) 10427–10430, <https://doi.org/10.1039/C8CC06334F>.
- [13] M. Natali, F. Nastasi, F. Puntiliero, A. Sartorel, Mechanistic insights into light-activated catalysis for water oxidation, *Eur. J. Inorg. Chem.* 2019 (2019) 2027–2039, <https://doi.org/10.1002/ejic.201801236>.
- [14] B. Matt, J. Fize, J. Moussa, H. Amouri, A. Pereira, V. Artero, G. Izzet, A. Proust, Charge photo-accumulation and photocatalytic hydrogen evolution under visible light at an iridium(III)-photosensitized polyoxotungstate, *Energy Environ. Sci.* 6 (2013) 1504–1508, <https://doi.org/10.1039/C3EE40352A>.
- [15] Y. Cao, Q. Chen, C. Shen, L. He, Polyoxometalate-based catalysts for CO₂ conversion, *Molecules* 24 (2019) 2069, <https://doi.org/10.3390/molecules24112069>.
- [16] J. Gu, W. Chen, G.-G. Shan, G. Li, C. Sun, X.-L. Wang, Z. Su, The roles of polyoxometalates in photocatalytic reduction of carbon dioxide, *Mater. Today Energy* 21 (2021) 100760, <https://doi.org/10.1016/j.mtener.2021.100760>.
- [17] M. Girardi, S. Blanchard, S. Griveau, P. Simon, M. Fontecave, F. Bediou, A. Proust, Electro-assisted reduction of CO₂ to CO and formaldehyde by (TOA)₆α-SiW₁₁O₃₉Co(+) polyoxometalate, *Eur. J. Inorg. Chem.* 2015 (2015) 3642–3648, <https://doi.org/10.1002/ejic.201500389>.
- [18] M. Girardi, D. Platzer, S. Griveau, F. Bediou, S. Alves, A. Proust, S. Blanchard, Assessing the electrocatalytic properties of the Cp^{*}Rh^{III+2-}-polyoxometalate derivative [H₂PW₁₁O₃₉Rh^{III}]Cp^{*}(OH₂)³⁻ towards CO₂ reduction, *Eur. J. Inorg. Chem.* 2019 (2019) 387–393, <https://doi.org/10.1002/ejic.201800454>.
- [19] B. Fabre, C. Falaise, E. Cadot, Polyoxometalates-functionalized electrodes for (photo)electrocatalytic applications: recent advances and prospects, *ACS Catal.* (2022), <https://doi.org/10.1021/acscatal.2c01847>.
- [20] A.M. Khenkin, I. Efremenko, L. Weiner, J.M.L. Martin, R. Neumann, Photochemical reduction of carbon dioxide catalyzed by a ruthenium-substituted polyoxometalate, *Chem. – Eur. J.* 16 (2010) 1356–1364, <https://doi.org/10.1002/chem.200901673>.
- [21] C. Ci, J.J. Carbó, R. Neumann, C.D. Graaf, J.M. Poblet, Photoreduction mechanism of CO₂ to CO catalyzed by a rhodium(I)-polyoxometalate hybrid compound, *ACS Catal.* 6 (2016) 6422–6428, <https://doi.org/10.1021/acscatal.6b01638>.
- [22] L. Qiao, M. Song, A. Geng, S. Yao, Polyoxometalate-based high-nuclear cobalt–vanadium–oxo cluster as efficient catalyst for visible light-driven CO₂ reduction, *Chin. Chem. Lett.* 30 (2019) 1273–1276, <https://doi.org/10.1016/j.clet.2019.01.024>.
- [23] Y. Chen, Z.-W. Guo, Y.-P. Chen, Z.-Y. Zhuang, G.-Q. Wang, X.-X. Li, S.-T. Zheng, G.-Y. Yang, Two novel nickel cluster substituted polyoxometalates: syntheses, structures and their photocatalytic activities, magnetic behaviors, and proton conduction properties, *Inorg. Chem. Front.* 8 (2021) 1303–1311, <https://doi.org/10.1039/DQQ101410A>.
- [24] G. Zhang, F. Wang, T. Tubul, M. Baranov, N. Leffler, A. Neyman, J.M. Poblet, I. A. Weinstock, Complexed semiconductor cores activate hexaniobate ligands as nucleophilic sites for solar-light reduction of CO₂ by water, *Angew. Chem. Int. Ed.* 61 (2022), <https://doi.org/10.1002/anie.202213162>.
- [25] Q. Chang, X. Meng, W. Ruan, Y. Feng, R. Li, J. Zhu, Y. Ding, H. Lv, W. Wang, G. Chen, X. Fang, Metal–organic cages with {SiW₉Ni₄} polyoxotungstate nodes, *Angew. Chem. Int. Ed.* 61 (2022), <https://doi.org/10.1002/anie.202117637>.
- [26] D. Zang, H. Wang, Polyoxometalate-based nanostructures for electrocatalytic and photocatalytic CO₂ reduction, *Polyoxometalates* 1 (2022) 9140006, <https://doi.org/10.26599/POM.2022.9140006>.
- [27] X.-X. Li, J. Liu, L. Zhang, L.-Z. Dong, Z.-F. Xin, S.-L. Li, X.-Q. Huang-Fu, K. Huang, Y.-Q. Lan, Hydrophobic polyoxometalate-based metal–organic framework for efficient CO₂ photoconversion, *ACS Appl. Mater. Interfaces* (2019) 6.
- [28] S.-L. Xie, J. Liu, L.-Z. Dong, S.-L. Li, Y.-Q. Lan, Z.-M. Su, Hetero-metallic active sites coupled with strongly reductive polyoxometalate for selective photocatalytic CO₂ to CH₄ conversion in water, *Chem. Sci.* 10 (2019) 185–190, <https://doi.org/10.1039/C8SC03471K>.
- [29] H. Xu, S. You, Z. Lang, Y. Sun, C. Sun, J. Zhou, X. Wang, Z. Kang, Z. Su, Highly efficient photoreduction of low-concentration CO₂ to syngas by using a polyoxometalates/rui composite, *Chem. – Eur. J.* 26 (2020) 2735–2740, <https://doi.org/10.1002/chem.201905155>.
- [30] Y. Benseghir, A. Solé-Daura, P. Mialane, J. Marrot, L. Dalecky, S. Béchu, M. Frégnaux, M. Gomez-Mingot, M. Fontecave, C. Mellot-Draznieks, A. Dolbecq, Understanding the photocatalytic reduction of CO₂ with heterometallic molybdenum(V) phosphate polyoxometalates in aqueous media, *ACS Catal.* 12 (2022) 453–464, <https://doi.org/10.1021/acscatal.1c04530>.
- [31] J. Du, Y.-Y. Ma, W.-J. Cui, S.-M. Zhang, Z.-G. Han, R.-H. Li, X.-Q. Han, W. Guan, Y.-H. Wang, Y.-Q. Li, Y. Liu, F.-Y. Yu, K.-Q. Wei, H.-Q. Tan, Z.-H. Kang, Y.-G. Li, Unraveling photocatalytic electron transfer mechanism in polyoxometalate-encapsulated metal–organic frameworks for high-efficient CO₂ reduction reaction, *Appl. Catal. B Environ.* 318 (2022) 121812, <https://doi.org/10.1016/j.apcatb.2022.121812>.
- [32] H. Lv, W. Guo, K. Wu, Z. Chen, J. Bacsa, D.G. Musaev, Y.V. Geletii, S.M. Lauinger, T. Lian, C.L. Hill, A noble-metal-free, tetra-nickel polyoxotungstate catalyst for efficient photocatalytic hydrogen evolution, *J. Am. Chem. Soc.* 136 (2014) 14015–14018, <https://doi.org/10.1021/ja5084078>.

[33] K. vonAllmen, R. Moré, R. Müller, J. Soriano-López, A. Linden, G.R. Patzke, Nickel-containing Keggin-type polyoxometalates as hydrogen evolution catalysts: photochemical structure–activity relationships, *ChemPlusChem* 80 (2015) 1389–1398, <https://doi.org/10.1002/cplu.201500074>.

[34] H. Lv, Y. Chi, J. vanLeusen, P. Kögerler, Z. Chen, J. Bacsa, Y.V. Geletii, W. Guo, T. Lian, C.L. Hill, $[(\text{Ni}_4(\text{OH})_3\text{AsO}_4)_4(\text{B}-\alpha\text{-PW}_9\text{O}_{34})_4]^{28-}$: a new polyoxometalate structural family with catalytic hydrogen evolution activity, *Chem. - Eur. J.* 21 (2015) 17363–17370, <https://doi.org/10.1002/chem.201503010>.

[35] X.-B. Han, C. Qin, X.-L. Wang, Y.-Z. Tan, X.-J. Zhao, E.-B. Wang, Bio-inspired assembly of cubane-adjustable polyoxometalate-based high-nuclear nickel clusters for visible light-driven hydrogen evolution, *Appl. Catal. B Environ.* 211 (2017) 349–356, <https://doi.org/10.1016/j.apcatb.2017.04.057>.

[36] G. Paille, A. Boulmier, A. Bensaïd, M.-H. Ha-Thi, T.-T. Tran, T. Pino, J. Marrot, E. Rivière, C.H. Hendon, O. Oms, M. Gomez-Mingot, M. Fontecave, C. Mellot-Draznieks, A. Dolbecq, P. Mialane, An unprecedented $(\text{Ni}_4\text{SiW}_9)$ hybrid polyoxometalate with high photocatalytic hydrogen evolution activity, *Chem. Commun.* 55 (2019) 4166–4169, <https://doi.org/10.1039/C9CC01269A>.

[37] L. Qin, R. Wang, X. Xin, M. Zhang, T. Liu, H. Lv, G.-Y. Yang, A dual-functional supramolecular assembly for enhanced photocatalytic hydrogen evolution, *Appl. Catal. B Environ.* 312 (2022) 121386, <https://doi.org/10.1016/j.apcatb.2022.121386>.

[38] E. Tanuhadi, J. Cano, S. Batool, A. Cherevan, D. Eder, A. Rompel, Ni12 tetracobane cores with slow relaxation of magnetization and efficient charge utilization for photocatalytic hydrogen evolution, *J. Mater. Chem. C.* 10 (2022) 17048–17052, <https://doi.org/10.1039/D2TC03508A>.

[39] C. Pichon, P. Mialane, A. Dolbecq, J. Marrot, E. Rivière, B.S. Bassil, U. Kortz, B. Keita, L. Nadjo, F. Sécheresse, Octa- and nonanuclear nickel(II) polyoxometalate clusters: synthesis and electrochemical and magnetic characterizations, *Inorg. Chem.* 47 (2008) 11120–11128, <https://doi.org/10.1021/ic801431f>.

[40] H. ElMoll, G. Rousseau, A. Dolbecq, O. Oms, J. Marrot, M. Haouas, F. Taulelle, E. Rivière, W. Wernsdorfer, D. Lachkar, E. Lacôte, B. Keita, P. Mialane, Properties of a tunable multinuclear nickel polyoxotungstate platform, *Chem. Eur. J.* 19 (2013) 6753–6765, <https://doi.org/10.1002/chem.201204366>.

[41] M.J. Frisch, G.W. Trucks, H.B. Schlegel, G.E. Scuseria, M.A. Robb, J.R. Cheeseman, G. Scalmani, V. Barone, G.A. Petersson, H. Nakatsuji, X. Li, M. Caricato, A. Marenich, J. Bloino, B.G. Janesko, R. Gomperts, B. Mennucci, H.P. Hratchian, J. V. Ortiz, A.F. Izmaylov, J.L. Sonnenberg, D. Williams-Young, F. Ding, F. Lipparini, F. Egidi, J. Goings, B. Peng, A. Petrone, T. Henderson, D. Ranasinghe, V. Zakrzewski, J. Gao, N. Rega, G. Zheng, W. Liang, M. Hada, M. Ehara, K. Toyota, R. Fukuda, J. Hasegawa, M. Ishida, T. Nakajima, Y. Honda, O. Kitao, H. Nakai, T. Vreven, K. Throssell, J.A. Montgomery Jr., J.E. Peralta, F. Ogliaro, M. Bearpark, J.J. Heyd, E.N. Brothers, K.N. Kudin, V.N. Staroverov, T.A. Keith, R. Kobayashi, J. Normand, K. Raghavachari, A.P. Rendell, J.C. Burant, S.S. Iyengar, J. Tomasi, M. Cossi, J.M. Millam, M. Klene, C. Adamo, R. Cammi, J.W. Ochterski, R.L. Martin, K. Morokuma, O. Farkas, J.B. Foresman, D.J. Fox, Gaussian 16, Revision C.02, Gaussian, Inc., Wallingford CT, 2016.

[42] P.J. Hay, W.R. Wadt, Ab initio effective core potentials for molecular calculations. Potentials for the transition metal atoms Sc to Hg, *J. Chem. Phys.* 82 (1985) 270–283, <https://doi.org/10.1063/1.448799>.

[43] A.W. Ehlers, M. Böhme, S. Dapprich, A. Göbbi, A. Höllwarth, V. Jonas, K.F. Köhler, R. Stegmann, A. Veldkamp, G. Frenking, A set of f-polarization functions for pseudo-potential basis sets of the transition metals Sc–Cu, Y–Ag and La–Au, *Chem. Phys. Lett.* 208 (1993) 111–114, [https://doi.org/10.1016/0009-2614\(93\)80086-5](https://doi.org/10.1016/0009-2614(93)80086-5).

[44] M.M. Francil, W.J. Pietro, W.J. Hehre, J.S. Binkley, M.S. Gordon, D.J. DeFrees, J. A. Pople, Self-consistent molecular orbital methods. XXII. A polarization-type basis set for second-row elements, *J. Chem. Phys.* 77 (1982) 3654–3665, <https://doi.org/10.1063/1.444267>.

[45] P.C. Hariharan, J.A. Pople, The influence of polarization functions on molecular orbital hydrogenation energies, *Theor. Chim. Acta* 28 (1973) 213–222, <https://doi.org/10.1007/BF00533485>.

[46] W.J. Hehre, R. Ditchfield, J.A. Pople, Self-consistent molecular orbital methods. XII. Further extensions of Gaussian-type basis sets for use in molecular orbital studies of organic molecules, *J. Chem. Phys.* 56 (1972) 2257–2261, <https://doi.org/10.1063/1.1677527>.

[47] E. Cancès, B. Mennucci, J. Tomasi, A new integral equation formalism for the polarizable continuum model: theoretical background and applications to isotropic and anisotropic dielectrics, *J. Chem. Phys.* 107 (1997) 3032–3041, <https://doi.org/10.1063/1.474659>.

[48] M. Álvarez-Moreno, C. de Graaf, N. López, F. Maseras, J.M. Poblet, C. Bo, Managing the computational chemistry big data problem: the ioChem-BD platform, *J. Chem. Inf. Model.* 55 (2015) 95–103, <https://doi.org/10.1021/ci500593j>.

[49] A. Call, M. Cibian, K. Yamuchi, K. Sakai, Visible-light-driven reduction of CO_2 to CO in fully aqueous media using a water-soluble cobalt porphyrin, *Sustain. Energy Fuels* 6 (2022) 2160–2164, <https://doi.org/10.1039/D2SE00291D>.

[50] X. Chai, H.-H. Huang, H. Liu, Z. Ke, W.-W. Yong, M.-T. Zhang, Y.-S. Cheng, X.-W. Wei, L. Zhang, G. Yuan, Highly efficient and selective photocatalytic CO_2 to CO conversion in aqueous solution, *Chem. Commun.* 56 (2020) 3851–3854, <https://doi.org/10.1039/D0CC00879F>.

[51] R. Gueret, L. Pouillard, M. Oshinowo, J. Chauvin, M. Dahmane, G. Dupeyre, P. P. Lainé, J. Fortage, M.-N. Collomb, Challenging the $[\text{Ru}(\text{bpy})_3]^{2+}$ photosensitizer with a triazatriangulenium robust organic dye for visible-light-driven hydrogen production in water, *ACS Catal.* 8 (2018) 3792–3802, <https://doi.org/10.1021/acscatal.7b04000>.

[52] M. Li, B. Zhuang, Y. Lu, L. An, Z.-G. Wang, Salt-induced liquid–liquid phase separation: combined experimental and theoretical investigation of water-acetonitrile–salt mixtures, *J. Am. Chem. Soc.* 143 (2021) 773–784, <https://doi.org/10.1021/jacs.0c09420>.

[53] R.N. Sampaio, D.C. Grills, D.E. Polansky, D.J. Szalda, E. Fujita, Unexpected roles of triethanolamine in the photochemical reduction of CO_2 to formate by ruthenium complexes, *J. Am. Chem. Soc.* 126 (2020).

[54] S.A. Jafari, M.H. Entezari, Salting out in ACN/water systems: Hofmeister effects and partition of quercetin, *J. Mol. Liq.* 312 (2020) 113331, <https://doi.org/10.1016/j.molliq.2020.113331>.

[55] A. Misra, K. Kozma, C. Streb, M. Nyman, Beyond charge balance: counter-cations in polyoxometalate chemistry, *Angew. Chem. Int. Ed.* 59 (2020) 596–612, <https://doi.org/10.1002/anie.201905600>.

[56] Y. Benseghir, A. Sole-Daura, D.R. Cairnie, A.L. Robinson, M. Duguet, P. Mialane, P. Gairola, M. Gomez-Mingot, M. Fontecave, D. Iovan, B. Bonnett, A.J. Morris, A. Dolbecq, C. Mellot-Draznieks, Unveiling the mechanism of the photocatalytic reduction of CO_2 to formate promoted by porphyrinic Zr-based metal–organic frameworks, *J. Mater. Chem. A.* 10 (2022) 18103–18115, <https://doi.org/10.1039/D2TA04164B>.

[57] Y. Pellegrin, F. Odobel, Sacrificial electron donor reagents for solar fuel production, *Comptes Rendus Chim.* 20 (2017) 283–295, <https://doi.org/10.1016/j.crci.2015.11.026>.

[58] J.-Y. Chen, L. Vilà-Nadal, A. Solé-Daura, G. Chisholm, T. Minato, C. Busche, T. Zhao, B. Kandasamy, A.Y. Ganin, R.M. Smith, I. Colliard, J.J. Carbó, J.M. Poblet, M. Nyman, L. Cronin, Effective storage of electrons in water by the formation of highly reduced polyoxometalate clusters, *J. Am. Chem. Soc.* 144 (2022) 8951–8960, <https://doi.org/10.1021/jacs.1c10584>.

[59] W. Song, M.K. Brennaman, J.M. Concepcion, J.W. Jurss, P.G. Hoertz, H. Luo, C. Chen, K. Hansson, T.J. Meyer, Interfacial electron transfer dynamics for $[\text{Ru}(\text{bpy})_2(4,4'\text{-PO}_3\text{H}_2)_2\text{bipy}]^{2+}$ sensitized TiO_2 in a dye-sensitized photoelectrosynthesis cell: factors influencing efficiency and dynamics, *J. Phys. Chem. C.* 115 (2011) 7081–7091, <https://doi.org/10.1021/jp200124k>.

[60] S.G. Cohen, A. Parola, G.H. Parsons, Photoreduction by amines, *Chem. Rev.* 73 (1973) 141–161, <https://doi.org/10.1021/cr60282a004>.

[61] S.G. Cohen, R.J. Baumgarten, Photoreduction of benzophenone by amines. photochemical oxidative deamination1, *J. Am. Chem. Soc.* 87 (1965) 2996–2997, <https://doi.org/10.1021/ja01091a032>.

[62] P.J. DeLaive, T.K. Foreman, C. Giannotti, D.G. Whitten, Photoinduced electron transfer reactions of transition-metal complexes with amines. Mechanistic studies of alternate pathways to back electron transfer, *J. Am. Chem. Soc.* 102 (1980) 5627–5631, <https://doi.org/10.1021/ja00537a037>.

[63] M. Stanbury, J.-D. Compaïn, S. Chardon-Noblat, Electro and photoreduction of CO_2 driven by manganese-carbonyl molecular catalysts, *Coord. Chem. Rev.* 361 (2018) 120–137, <https://doi.org/10.1016/j.ccr.2018.01.014>.

[64] P.A. Davethu, S.P. de Visser, CO_2 reduction on an iron-porphyrin center: a computational study, *J. Phys. Chem. A.* 123 (2019) 6527–6535, <https://doi.org/10.1021/acs.jpca.9b05102>.

[65] J. Shakeri, H. Farrokhpour, H. Hadadzadeh, M. Josaghani, Photoreduction of CO_2 to CO by a mononuclear Re(I) complex and DFT evaluation of the photocatalytic mechanism, *RSC Adv.* 5 (2015) 41125–41134, <https://doi.org/10.1039/C5RA02002F>.

[66] F. Wang, B. Cao, W.-P. To, C.-W. Tse, K. Li, X.-Y. Chang, C. Zang, S.L.-F. Chan, C.-M. Che, The effects of chelating N4 ligand coordination on Co(II)-catalysed photochemical conversion of CO_2 to CO: reaction mechanism and DFT calculations, *Catal. Sci. Technol.* 6 (2016) 7408–7420, <https://doi.org/10.1039/C6CY01265E>.

[67] F. Wang, R. Neumann, C. de Graaf, J.M. Poblet, Photoreduction mechanism of CO_2 to CO catalyzed by a three-component hybrid construct with a bimetallic rhodium catalyst, *ACS Catal.* (2021) 1495–1504, <https://doi.org/10.1021/acscatal.0c04366>.

[68] Z.-H. Yan, B. Ma, S.-R. Li, J. Liu, R. Chen, M.-H. Du, S. Jin, G.-L. Zhuang, L.-S. Long, X.-J. Kong, L.-S. Zheng, Encapsulating a Ni(II) molecular catalyst in photoactive metal–organic framework for highly efficient photoreduction of CO_2 , *Sci. Bull.* 64 (2019) 976–985, <https://doi.org/10.1016/j.scib.2019.05.014>.

[69] C.-Y. Zhu, Y.-Q. Zhang, R.-Z. Liao, W. Xia, J.-C. Hu, J. Wu, H. Liu, F. Wang, Photocatalytic reduction of CO_2 to CO and formate by a novel Co(II) catalyst containing a cis-oxygen atom: photocatalysis and DFT calculations, *Dalton Trans.* 47 (2018) 13142–13150, <https://doi.org/10.1039/C8DT02148A>.

[70] J. Shen, M.J. Kolb, A.J. Göttle, M.T.M. Koper, DFT study on the mechanism of the electrochemical reduction of CO_2 catalyzed by cobalt porphyrins, *J. Phys. Chem. C.* 120 (2016) 15714–15721, <https://doi.org/10.1021/acs.jpcc.5b10763>.

[71] M. Isogawa, A.K. Sharma, CO_2 reduction by a Mn electrocatalyst in the presence of a Lewis acid: a DFT study on the reaction mechanism, *Sustain. Energy Fuels* 3 (2019) 1730–1738, <https://doi.org/10.1039/C9SE00213H>.